Acta Crystallographica Section D
Biological Crystallography
ISSN 0907-4449

Physical and structural studies on the cryocooling of insulin crystals

Ardeschir Vahedi-Faridi,[a]†‡ Jeffrey Lovelace,[b]† Henry D. Bellamy,[c]§ Edward H. Snell[d] and Gloria E. O. Borgstahl[b]*

[a]The University of Toledo, Department of Chemistry, 2801 West Bancroft Street, Toledo, OH 43606, USA, [b]Eppley Institute for Cancer Research, 987696 Nebraska Medical Center, Omaha, NE 68198-7696, USA, [c]Stanford Synchrotron Radiation Laboratory, 2575 Sand Hill Road, Menlo Park, CA 94025, USA, and [d]NASA Laboratory for Structural Biology, Code SD46, Marshall Space Flight Center, Huntsville, AL 35812, USA

† These authors contributed equally to this work.
‡ Present address: Brown University, Department of Molecular Biology, J. W. Wilson Laboratory, Box G-J2, Providence, RI 02912, USA.
§ Present address: Center for Advanced Microstructures and Devices, Louisiana State University, 6980 Jefferson Highway, Baton Rouge, LA 70806, USA.

Correspondence e-mail: gborgstahl@unmc.edu

© 2003 International Union of Crystallography
Printed in Denmark – all rights reserved

Received 25 April 2003
Accepted 5 September 2003

Reflection profiles were analyzed from microgravity-grown (μ*g*) and earth-grown insulin crystals to measure mosaicity (η) and to reveal mosaic domain structure and composition. The effects of cryocooling on single-domain and multi-domain crystals were compared. The effects of cryocooling on insulin structure were also re-examined. Microgravity crystals were of larger volume, were more homogeneous and were of higher quality than earth crystals. Several μ*g* crystals contained a single mosaic domain which encompassed all or nearly all of the crystal with an η_{avg} of 0.005°. The earth crystals varied in quality and all contained multiple domains with an η_{avg} of 0.031°. Cryocooling caused a 43-fold increase in η for μ*g* crystals (η_{avg} = 0.217°) and an eightfold increase for earth crystals (η_{avg} = 0.246°). These results indicate that very well ordered crystals are not completely protected from the stresses associated with cryocooling, especially when structural perturbations occur. However, there were differences in the reflection profiles. For multi-mosaic domain crystals, each domain individually broadened and separated from the other domains upon cryocooling. Cryocooling did not cause an increase in the number of domains. A crystal composed of a single domain retained this domain structure and the reflection profiles simply broadened. Therefore, an improved signal-to-noise ratio for each reflection was measured from cryocooled single-domain crystals relative to cryocooled multi-domain crystals. The improved signal from μ*g* crystals, along with the increase in crystal size, facilitated the measurement of the weaker high-resolution reflections. The observed broadening of reflection profiles indicates increased variation in unit-cell parameters, which may be linked to cryocooling-associated structural changes and disorder.

1. Introduction

Cryocrystallography is a dominant technique used to aid data collection in macromolecular crystallography (Garman & Schneider, 1997; Rodgers, 1997). Cryocooling extends the lifetime of crystals in the X-ray beam by greatly reducing radiation damage, which can rapidly degrade high-resolution data (Mitchell & Garman, 1994; Rodgers, 1994). Cryocooling also leads to improved structural resolution by decreasing atomic thermal vibration. In studies on rhombohedral insulin crystals, the highest resolution room-temperature (rt) structure is at 1.5 Å resolution and a cryocooled (cryo) structure was determined at 1.0 Å resolution (Baker *et al.*, 1988; Smith *et al.*, 2003). In this case, it is not clear that cryocooling accounted for the majority of this increase in resolution as there were also differences in crystal-growth conditions (earth *versus* microgravity, μ*g*), crystal size and X-ray instrumentation (sealed tube *versus* rotating anode). In the research

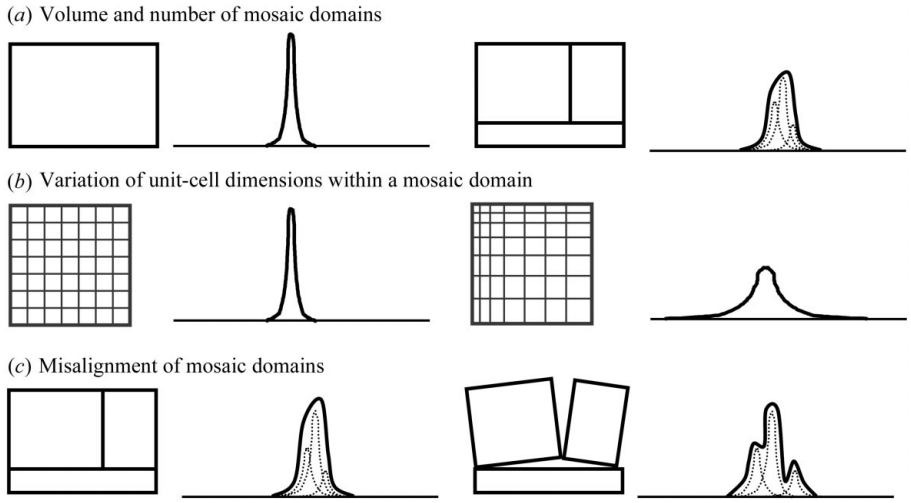

Figure 1
Schematic drawing of the mosaic domain model applied to reflection profiles.

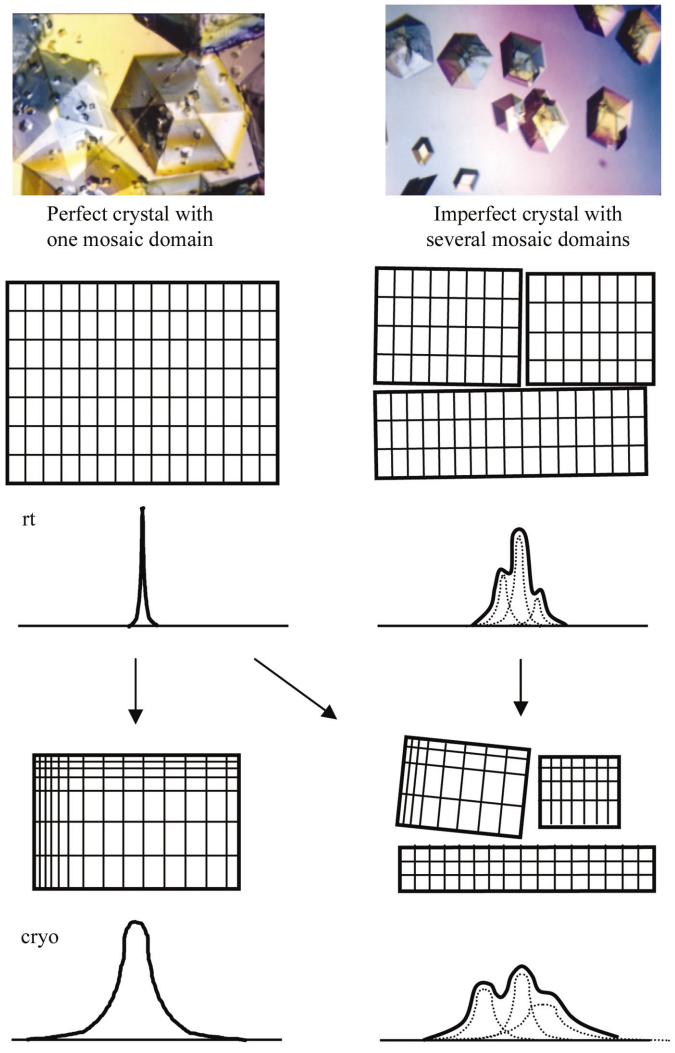

Figure 2
Theoretical effects of cryocooling on crystal mosaicity of hypothetically perfect and imperfect crystals and the application of the mosaic domain model to reflection profiles. Pictures of the μg and earth insulin crystals used in this study are at the top (adapted from Borgstahl *et al.*, 2001).

presented here, diffraction resolution, reflection profiles and mosaicity data were collected on μg and earth-grown crystals with the X-ray source constant in order to help separate these effects.

An unfortunate drawback of cryocooling is the dramatic increase in crystal mosaicity that is frequently observed (Kriminski *et al.*, 2002; Mitchell & Garman, 1994; Rodgers, 1994; Teng, 1998). To study this increase in mosaicity, it is useful to review the theory which describes the mosaic nature of crystals. Darwin described crystals as a mosaic of multiple crystalline domains (Darwin, 1922). The angular spread between domains (ω), domain size (s) and variation in unit-cell dimensions (δa) affect the measured mosaic spread (Boggon *et al.*, 2000; Nave, 1998). The depiction of these domains as discrete blocks or volumes within the crystal in Fig. 1 is an oversimplification. Domains are not necessarily block structures and a single crystal may contain many domains. The theory does not address boundary regions between domains. A hypothetically perfect crystal (Fig. 1 and Fig. 2, left) is composed of a single domain and has infinitesimally small reciprocal-lattice points. The reflection profile is correspondingly narrow and is broadened only by Fourier truncation effects arising from the finite crystal size. For an imperfect crystal (Figs. 1 and Fig. 2, right) with several mosaic domains and misalignment between them, each mosaic domain contributes an individual rocking profile (dotted curves) to the complete reflection profile (solid curves) (Helliwell, 1988). Within a single crystal, an increase in the number of domains or decrease in the domain volume causes profile broadening owing to Fourier truncation effects (Fig. 1*a*). Any variation of the unit-cell dimensions within a given domain will also broaden the profile (Fig. 1*b*). In addition, misalignment of these domains with respect to each other causes a broadening of each reflection owing to the corresponding divergence or misalignment of the diffracted beams contributed by each domain (Fig. 1*c*). Real crystals are affected by a combination of these factors.

In typical data collection, geometrical and spectral effects mask the mosaic nature of the crystal. The observed reflection profile is typically smeared by the divergence and energy dispersion of the X-ray beam. It is also broadened by diffraction geometry, *e.g.* the Lorentz effect. Common data-processing software give a mosaicity value that is normally defined as the smallest angle through which a crystal can rotate such that a reflection is fully recorded (Leslie, 1999; Otwinowski & Minor, 2001). This estimate of mosaicity is needed for data collection and processing, but it does not represent the mosaicity arising from the physical parameters of the crystal alone. To examine this intrinsic mosaicity, a nearly parallel monochromatic radiation source has to be used, *e.g.* unfocused synchrotron radiation. The spectral and

Table 1
Fine φ-slicing data-collection statistics for insulin crystals.

Crystal	Date†	X-ray exposure time (s)	$\Delta\varphi$‡ (°)	No. of data frames	Temperature (K)
Microgravity-grown insulin crystals					
µg1	12/98	5	0.001	1000	298
µg2	12/98	5	0.001	1000	298
µg3	12/98	2	0.001	500	298
µg4	7/99	2	0.001	2000	298
µg5	7/99	2	0.001	2000	298
µg6	7/99	2	0.001	2000	298
cr-µg6	7/99	2	0.005	1998	100
cr-µg7	4/99	5	0.005	1596	100
cr-µg8	4/99	5	0.010	1596	100
cr-µg9	7/99	5	0.005	1998	100
Earth-grown insulin crystals					
earth1	12/98	5	0.001	2000	298
earth2	12/98	2	0.001	500	298
earth3	12/98	2	0.001	2000	298
earth4	7/99	5	0.001	2000	298
cr-earth4	7/99	2	0.005	1998	100
earth5	7/99	5	0.001	1999	298
earth6	7/99	5	0.001	2000	298
cr-earth7	4/99	6	0.010	1996	100
cr-earth8	4/99	8	0.010	1858	100
cr-earth9	4/99	15	0.010	467	100

† For the 12/98 and 4/99 data, $\Delta\lambda/\lambda = 2.43 \times 10^{-4}$, vertical beam divergence (σ_v) = 0.0011° and horizontal beam divergence (σ_h) = 0.0028°. For the 7/99 data, $\Delta\lambda/\lambda = 1.94 \times 10^{-4}$, σ_v = 0.0009° and σ_h = 0.0025°. Preliminary data on rt crystals, including approximations to the crystal volumes, have been reported previously (Borgstahl *et al.*, 2001). ‡ Size of the fine φ-slices taken as stills.

geometric parameters are then sufficiently small that details of the mosaic structure can be extracted from the reflection profile and an accurate measure of the mosaicity made by deconvolution of those same parameters. A fine φ-slicing method using highly monochromatic and parallel synchrotron radiation and a CCD area detector has been developed to accurately measure hundreds of reflection profiles in a short time (Bellamy *et al.*, 2000). The mosaicity η is deconvoluted from the measured angular width of each profile φ_R by applying corrections for the beam parameters and the Lorentz factor (Bellamy *et al.*, 2000; Colapietro *et al.*, 1992; Greenhough & Helliwell, 1982). The number of mosaic domains can be estimated from curve-fitting the complete reflection profile (Otálora *et al.*, 1999) and from this analysis some information on the angular separation (ω) between domains can be measured. When reflection profiles are collected and analyzed in this way, a model of the mosaic domain structure and the composition of a crystal can be described for comparative purposes. Previously, this fine φ-slicing methodology has been used to measure reflection profiles and compare the mosaicity of rt µg- and earth-grown insulin crystals (Borgstahl *et al.*, 2001). The µg- and earth-grown insulin crystals provide populations of single-domain and multi-mosaic domain crystals that were used in this study to understand the effects of cryocooling on mosaic domain structure and diffraction quality.

Researchers have begun to study the structural effects of cryocooling in an effort to understand the typical increase in mosaicity associated with cryocooling. The general trends are that upon cryocooling the unit cell contracts 2–7%, repacks and the area of the protein surface involved in lattice contacts increases by as much as 50% (Deacon *et al.*, 1997; Juers & Matthews, 2001). In this research, the corresponding effects of cryocooling on insulin structure were re-examined. The relative contributions of crystal mosaic block structure and of cryocooling to diffraction quality were compared and correlated with changes in protein structure.

2. Methods

2.1. Crystal growth

*R*3 crystals of recombinant human insulin were grown with the Commercial Protein Crystallization Facility (PCF) during the nine-day STS-95 Space Shuttle Mission starting October 29, 1998. Crystals were grown by batch and nucleation in µ*g* was controlled by temperature as described in Long *et al.* (1996). This method of growth eliminates the deleterious effects of Marangoni convection observed when the more common vapor-diffusion methods are used in µ*g* (Chayen *et al.*, 1997). Earth crystals were grown at the same time in the same apparatus with insulin from the same batch. Prior to data collection, the crystals remained in their PCF bottles unopened at 295 K.

2.2. Cryocooling protocol

The following cryoprotection protocol was developed and optimized for insulin crystals by researchers at the Hauptmann–Woodward Institute. Insulin crystals were picked up in cryoloops (Hampton Research) and successively immersed into cryoprotectant solutions composed of the mother liquor the crystals grew in, diluted with glycerol to make solutions containing 5, 10, 20 and 30%(*v*/*v*) glycerol. A final soak of 25% glycerol, 15% PEG 300 was used as this has been found to effectively remove the ice rings observed without this step. Each soak lasted for approximately 30 s. The crystals were then flash-cooled in a 100 K nitrogen-gas stream provided by the SSRL-style cryocooler (Bellamy *et al.*, 1994).

2.3. Fine φ-sliced data collection

Stanford Synchrotron Radiation Laboratory (SSRL) bending-magnet beamline 1-5 was used (Bellamy *et al.*, 2000) in unfocused mode in order to minimize beam divergence (Table 1). The beam properties were calculated from the source size and the 0.3 mm beam-defining aperture 25.5 m from the source. For most of the data sets, the vertical and horizontal beam divergences were 0.0028 and 0.0011°, respectively, and $\Delta\lambda/\lambda$ was 2.43×10^{-4}. The values for the remaining data sets were slightly better and are noted in Table 1. Recent alterations to beamline 1-5 now prevent unfocusing. Rt data were collected from crystals mounted in capillaries as previously described (Borgstahl *et al.*, 2001). In order to obtain a statistically significant number of measurements in a reasonable amount of beamtime, data were collected with a Quantum-4 CCD detector (ADSC) using rotation-camera geometry as described previously (Bellamy *et al.*, 2000; Borgstahl *et al.*, 2001; Snell *et al.*, 2001). To determine

the crystal orientation, two orthogonal 8–10° swaths of coarse data were collected ($\Delta\varphi$ = 1° with 60 s exposure) and processed with *MOSFLM* (Powell, 1999). From each swath a 1.0° range was then selected and fine φ-sliced data corresponding to that range were collected for mosaicity measurements. For the cryo data, fine φ-sliced data were collected as stills spaced by 0.005 or 0.010° with 2, 5, 6, 8 or 15 s X-ray exposures (see Table 1). The crystal-to-detector distance was 170 mm and the diffraction resolution was 1.9 Å at the edge of the detector and 1.5 Å at the corner. The space group was *R*3, with unit-cell dimensions $a = b$ = 80.09–81.41, c = 33.15–34.28 Å when indexed hexagonally. The wavelength was 1.0 Å and the beam was collimated to 0.3 mm diameter for all measurements. The data were collected in constant-time mode and not corrected for the change in beam intensity with ring current. In general, the ring current decreased from 100 to 60 mA over a 24 h period between ring fills. Therefore, the change in beam intensity during the time a given reflection was illuminated was negligible.

2.4. Data processing

The fine φ-sliced data were processed and the reflection profiles were analyzed using *BEAM-ish* 2.0 (Lovelace & Borgstahl, 2003; Lovelace *et al.*, 2000). For each swath of data, *BEAM-ish* uses *MOSFLM* to process the coarse images and obtain the unit-cell dimensions and crystal-orientation matrix. *MOSFLM* produces a list of all the theoretically observable reflections and their expected positions. All the fine images for that swath are then integrated at the predicted reflection positions and background subtracted to obtain the reflection profiles (intensity *versus* φ) (Lovelace *et al.*, 2000). To reduce noise, the rt earth and cryo reflection profiles were smoothed with a traveling window that averaged the intensity over three images and then replaced the integrated intensity value with this average. In order to be accepted for profile analysis, the reflections had to have $I_{\max} > 100$ or 150 for earth and μg, respectively, and $I_{\max}/I_{\rm ave} > 5$. $I_{\max}$ was normalized to a 2 s X-ray exposure before the filter was applied. $I_{\rm ave}$ was defined as the average of all the integrated spot intensities at the reflection's predicted location on all the fine-φ images after removal of 'zingers' (Borgstahl *et al.*, 2001). Gaussian curves were fitted to the reflection profiles using a genetic algorithm (Wormington *et al.*, 1999). The mosaicity η was deconvoluted from the measured reflection full-width at half-maximum φ_R,

$$\eta = \frac{|\varphi_R| - (L^2\zeta^2\gamma_h^2 + \gamma_v^2)^{1/2}}{Ld^* \cos\theta_{hkl}} - \left(\frac{\delta\lambda}{\lambda}\right)\tan\theta_{hkl}, \qquad (1)$$

where γ_v and γ_h are the vertical and horizontal crossfire angles at the sample, $\delta\lambda/\lambda$ is the wavelength dispersion, L is the Lorentz correction, ζ is the position of the corresponding reciprocal-lattice point projected onto the rotation axis and $d^* = \lambda/d$ (where d is the resolution; $d = \lambda/2\sin\theta_{hkl}$). The derivation of this equation and the effects of these parameters on reflection broadening have been described previously (Bellamy *et al.*, 2000; Helliwell, 1992). The inter-process communication feature of *BEAM-ish* 2.0 was used to search for symmetry-related reflections across multiple data sets (Lovelace & Borgstahl, 2003; Lovelace *et al.*, 2000).

2.5. Three-dimensional topographs

The three-dimensional reflection topographs were generated using scripts written in *Matlab*. A range of frames was selected that encompassed the profile and for each detector frame a sub-image of 13 × 13 pixels centered on the reflection was extracted and the sub-images were stacked on top of each other to form a box. The dimensions of the box were 13 × 13 × (number of detector images). Pixels within the box were assigned two values. The first was a color which ranged from yellow (low intensities) to light blue (high intensities) based on the intensity of the original pixel. An α value was assigned to each color to indicate the transparency of a particular pixel and ranged from clear (low intensities) to solid (high intensities). This had the effect of making the background clear while making the reflection center more opaque. For visualization, the detector frames were assigned φ values and the pixel dimensions were converted into millimetres.

Three-dimensional reflection topographs were then converted to reciprocal (*hkl*) space following the algorithm previously briefly described (Powell, 1999). A detailed example is provided below to demonstrate the conversion based on files produced by *MOSFLM*. It is actually a three-part process. The following information is needed to complete the task: the crystal-to-detector distance (XtoD), the location of the reflection ($X_{\rm ref}$, $Y_{\rm ref}$ and $\text{Omega}_{\rm ref}$), the location of the beam center ($X_{\rm beam}$, $Y_{\rm beam}$), the wavelength (λ), the orientation matrix (A) and two *MOSFLM* parameters that are dependent on the type of detector and the orientation. The first depends on the crystal rotation axis with respect to how the detector images are read out (OmegaFD) and the second is based on the source location with respect to how the images are read out (InvertX). The orientation matrix A is stored as the first nine values in the *MOSFLM* *.mat file. For this example, an ADSC Quantum 4 detector was used. The experimental parameters were: XtoD = 170.0 mm, $X_{\rm ref}$ = 137.1 mm, $Y_{\rm ref}$ = 53 mm, $\text{Omega}_{\rm ref}$ = 284.16°, $X_{\rm beam}$ = 96.12 mm, $Y_{\rm beam}$ = 99.55 mm, λ = 1.0 Å. The following variables are detector-dependent: OmegaFD = 0°, InvertX = −1.

The orientation matrix A is

$$\begin{pmatrix} -0.00185754 & 0.00993757 & 0.00799710 \\ -0.00286203 & -0.00519506 & 0.02742667 \\ 0.01335349 & 0.00830231 & 0.00758963 \end{pmatrix}$$

and the target R_{hkl} = (−27, 16, −4).

Step 1. Convert from detector space to *MOSFLM* space.

$$\text{MS}_{\rm XYD} = \text{DS_to_MS} \cdot \text{DS} \qquad (2)$$

$$\text{DS} = \begin{pmatrix} X_{\rm ref} \\ Y_{\rm ref} \\ 1 \end{pmatrix}, \qquad (3)$$

$$\mathrm{DS_to_MS} = \begin{bmatrix} \mathrm{InvertX}\cdot\cos(\mathrm{OmegaFD}) & \sin(\mathrm{OmegaFD}) & 0 \\ -\mathrm{InvertX}\cdot\sin(\mathrm{OmegaFD}) & \mathrm{InvertX}\cdot\cos(\mathrm{OmegaFD}) & 0 \\ 0 & 0 & \mathrm{XtoD} \end{bmatrix} \begin{pmatrix} 1 & 0 & -X_{\mathrm{beam}} \\ 0 & 1 & -Y_{\mathrm{beam}} \\ 0 & 0 & 1 \end{pmatrix}. \quad (4)$$

Step 2. Use the MS vector to derive the reciprocal-space coordinate vector *xyz*.

$$\mathrm{MS}_{\mathrm{XYD}} = \begin{pmatrix} X \\ Y \\ D \end{pmatrix}, \quad (5)$$

$$xyz = \begin{pmatrix} \{X/[\lambda(X^2+Y^2+D^2)^{1/2}]\} \\ \{Y/[\lambda(X^2+Y^2+D^2)^{1/2}]\} \\ \{D/[\lambda(X^2+Y^2+D^2)^{1/2}]\} - (1/\lambda) \end{pmatrix}. \quad (6)$$

Step 3. Use the *xyz* and the orientation matrix A to calculate the reflection indices.

$$R_{hkl} = A^{-1}\cdot\mathrm{MS_to_A}\cdot\mathrm{Wave}\cdot\mathrm{Rotation}\cdot xyz, \quad (7)$$

$$\mathrm{MS_to_A} = \begin{pmatrix} 0 & 0 & 1 \\ 1 & 0 & 0 \\ 0 & 1 & 0 \end{pmatrix}, \quad (8)$$

$$\mathrm{Wave} = \begin{pmatrix} \lambda & 0 & 0 \\ 0 & \lambda & 0 \\ 0 & 0 & \lambda \end{pmatrix}, \quad (9)$$

$$\mathrm{Rotation} = \begin{bmatrix} \cos(\mathrm{Phi}_{\mathrm{ref}}) & 0 & -\sin(\mathrm{Phi}_{\mathrm{ref}}) \\ 0 & 1 & 0 \\ \sin(\mathrm{Phi}_{\mathrm{ref}}) & 0 & \cos(\mathrm{Phi}_{\mathrm{ref}}) \end{bmatrix}, \quad (10)$$

$$R_{hkl} = \begin{pmatrix} -26.983 \\ 16.019 \\ -3.942 \end{pmatrix}. \quad (11)$$

The MS_to_A matrix (8) transforms the coordinate space from *MOSFLM* to that used to generate the orientation matrix. The wave matrix (9) removes λ from the previous calculation in step 2 because λ is not included within the orientation matrix. The rotation matrix (10) describes a rotation about φ. After rounding, R_{hkl} is (−27, 16, −4) and agrees with the target value. Values within 0.15 of the actual indices are considered acceptable. In the conversion process of pixels into the *hkl* space, the results were not rounded in order to preserve the pixel positions in *hkl* space. No correction was applied for the broadening of the reflection topographs by the point-spread function of the CCD detector. However, this is about one pixel for the Quantum-4 so it should not appreciably affect the results.

3. Results and discussion

3.1. Theoretical framework

In this study, mosaic domain theory was applied to the interpretation of the reflection profiles measured from insulin crystals. The possible effects of cryocooling on the reflection profiles of hypothetically perfect and imperfect crystals are considered in Fig. 2. The perfect crystal is composed of only one mosaic domain and has an infinitesimally thin rocking curve (Fig. 2, left). Cryocooling typically causes the unit cell to shrink and this shrinkage may be irregular owing to the different cooling rates experienced by various parts of the crystal during the flash-cooling process (Snell *et al.*, 2002). This cryocooling-induced variation in unit-cell dimensions across the crystal will broaden the reflection profile (Fig. 2, bottom left). The stress induced by unit-cell shrinkage may increase the number of mosaic domains in the crystal (Fig. 2, center arrow). Since each domain contributes its own slightly misaligned profile to the overall reflection profile, any increase in the number of domains will broaden the reflection profile. These same effects are present in the cryocooling of an imperfect crystal, but the presence of several mosaic domains adds further complications (Fig. 2, right). The cryocooling-induced unit-cell shrinkage may cause the mosaic domains to separate from each other and become further misaligned. In addition, the unit cells within each domain are irregular in size and may differ between domains.

3.2. Characterization of rt insulin crystals

Fine φ-sliced diffraction data were collected on six rt earth, six rt μ*g*, four cryo earth and four cryo μ*g* crystals (Table 1). Mosaicity data were measured from the full-width at half-maximum (FWHM) and full-width at quarter-maximum (FWQM) of reflection profiles (defined in Fig. 3; Bellamy *et al.*, 2000). In an earlier report of the rt data, the μ*g*-grown insulin crystals were found to be very large and of superior diffraction quality when compared with the earth-grown crystals (Borgstahl *et al.*, 2001). The size analysis of the crystals was reported previously with linear dimensions ranging from 0.4 to 1.8 mm for μ*g* crystals and from 0.1 to 0.4 for earth crystals (see Table 1; Borgstahl *et al.*, 2001) and estimated crystal volumes are listed in Tables 2 and 3. The diffraction data are now reanalyzed with an $I_{\max}$ cutoff that was normalized for exposure time, which allows a comparison of diffraction resolution (see notes in Table 2) and examination in greater detail. The average mosaicity (η_{avg}) for μ*g* crystals was 0.005° FWHM and 0.007° FWQM (standard deviation = 0.002° for both; n = 6; Table 2); half of the crystals were resolved as primarily a single mosaic domain (Figs. 3*a*, 3*c* and 3*d*) and the rest were

composed of two mosaic domains (Figs. 3*b*, 3*e* and 3*f*). Crystal µ*g*4 was the best crystal, with only one mosaic domain that could be fitted with a single Gaussian curve (Fig. 3*d*) and an η_{avg} of 0.003° FWHM and 0.005° FWQM (standard devations of 0.001 and 0.002°, respectively; n = 483; Table 2). The µ*g* batch was composed of a fairly homogeneous population of crystals, with the η_{avg} of each crystal ranging from 0.003 to 0.007° FWHM and 0.005 to 0.009° FWQM. These crystals also had low individual standard deviations in η ranging from 0.001 to 0.005°, which indicated a low spread in the η values of individual reflections. At rt, the earth and µ*g* crystals were significantly different (T = 3.6261, two-tailed P = 0.0046). The earth crystals contained 3–4 mosaic domains (Fig. 4) and had a sixfold higher η_{avg} at FWHM and an eightfold higher η_{avg} at FWQM. These crystals had a fivefold higher individual standard deviations in η at FWHM and fivefold to 13-fold higher standard deviations at FWQM, which indicated a larger spread in the η values for reflections of a given crystal. The earth crystal with the best η, earth5, was composed of at least four mosaic domains with an η_{avg} of 0.013° FWHM and 0.024° FWQM (standard deviations of 0.004 and 0.007°, respectively; n = 95; Table 2). The best earth crystal at rt had threefold and fivefold higher η values than the best µ*g* crystal.

The effect of mosaicity and crystal volume is evident in the maximum intensity, or peak height, of the reflections and in the overall diffraction resolution of the crystal. Owing to the narrowness of the reflection widths and the larger crystal volume, the average maximum peak intensity (defined in Fig. 3; Bellamy *et al.*, 2000) calculated from all reflections for the µ*g* crystals was eightfold to 113-fold higher than the earth crystals

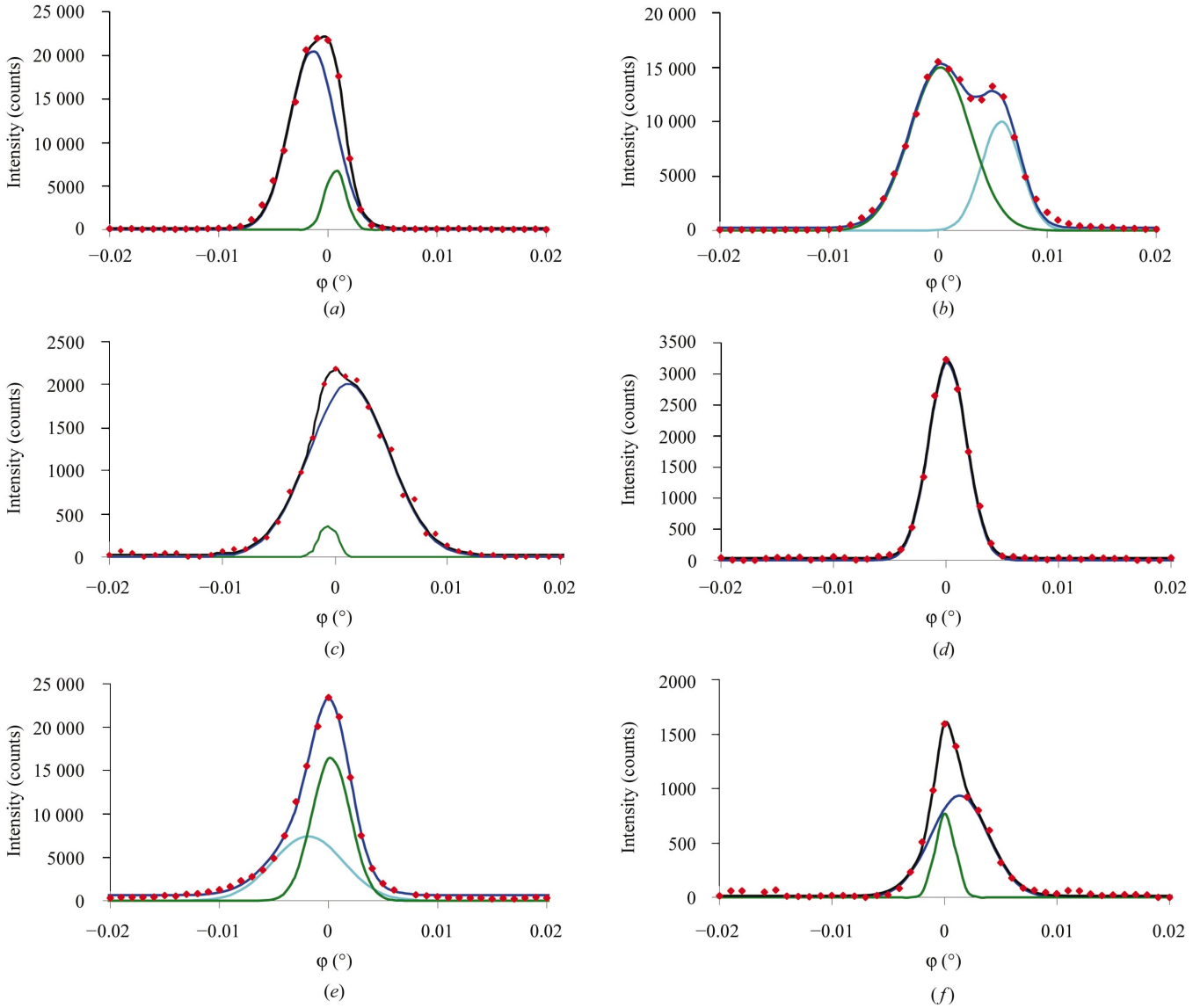

Figure 3
Representative reflection profiles from rt µ*g* crystals. Reflections were selected that had average resolution and average FWHM mosaicity for that crystal (see Table 2). (*a*) µg1 [−11, 29, −1], d = 2.83 Å, φ_R = 0.005°, η = 0.004°; (*b*) µg2 [−20, 19, −9], d = 2.64 Å, φ_R = 0.010°, η = 0.007°; (*c*) µg3 [−19, 17, −9], d = 2.73 Å, φ_R = 0.008°, η = 0.005°; (*d*) µg4 [9, −8, 11], d = 2.90 Å, φ_R = 0.004°, η = 0.003°; (*e*) µg5 [−25, 18, 5], d = 2.90 Å, φ_R = 0.005°, η = 0.004°; (*f*) µg6 [−23, 1, −6], d = 2.78 Å, φ_R = 0.004°, η = 0.003°.

(Table 2). The best μg crystal (μg4) had 20–40-fold greater maximum peak intensity than the best earth crystals (earth3 and earth5). This increase in signal-to-noise ratio allowed more of the weaker reflections to be detected from the μg crystals, including those of high resolution. All six rt μg crystals diffracted beyond the edge of the detector, with measured highest resolution reflections between 1.54 and 1.63 Å that correspond to this edge. The true resolution limit for the μg crystals was not measured because of time constraints. The resolution limit of the earth crystals ranged from 1.73 to 2.91 Å. It should be noted that the unfocused synchrotron beam used in these studies was relatively weak and also limited the resolution obtained from these crystals. It was concluded that the improvements in crystal quality and volume provided by growth in a μg environment resulted in an improvement in mosaicity and signal-to-noise ratio for the observed data and had the overall effect of extending the resolution of the data, enabling a more precise structure determination.

3.3. Characterization of cryo insulin crystals

Cryocooling had the overall effect of increasing the crystal mosaicity (Table 3). The η_{avg} for μg crystals increased 43-fold to 0.217° at FWHM (standard deviation 0.012°) and increased 53-fold to 0.370° at FWQM (standard deviation 0.069°). Presumably because they were already more disordered, the η_{avg} for earth crystals increased only sevenfold to eightfold to 0.246° FWHM (standard deviation 0.068°) and 0.391° FWQM (standard deviation 0.109°). The trend for the μg crystals to have lower mosaicity on average still holds, although the difference in the samples by this criterion alone is not statis-

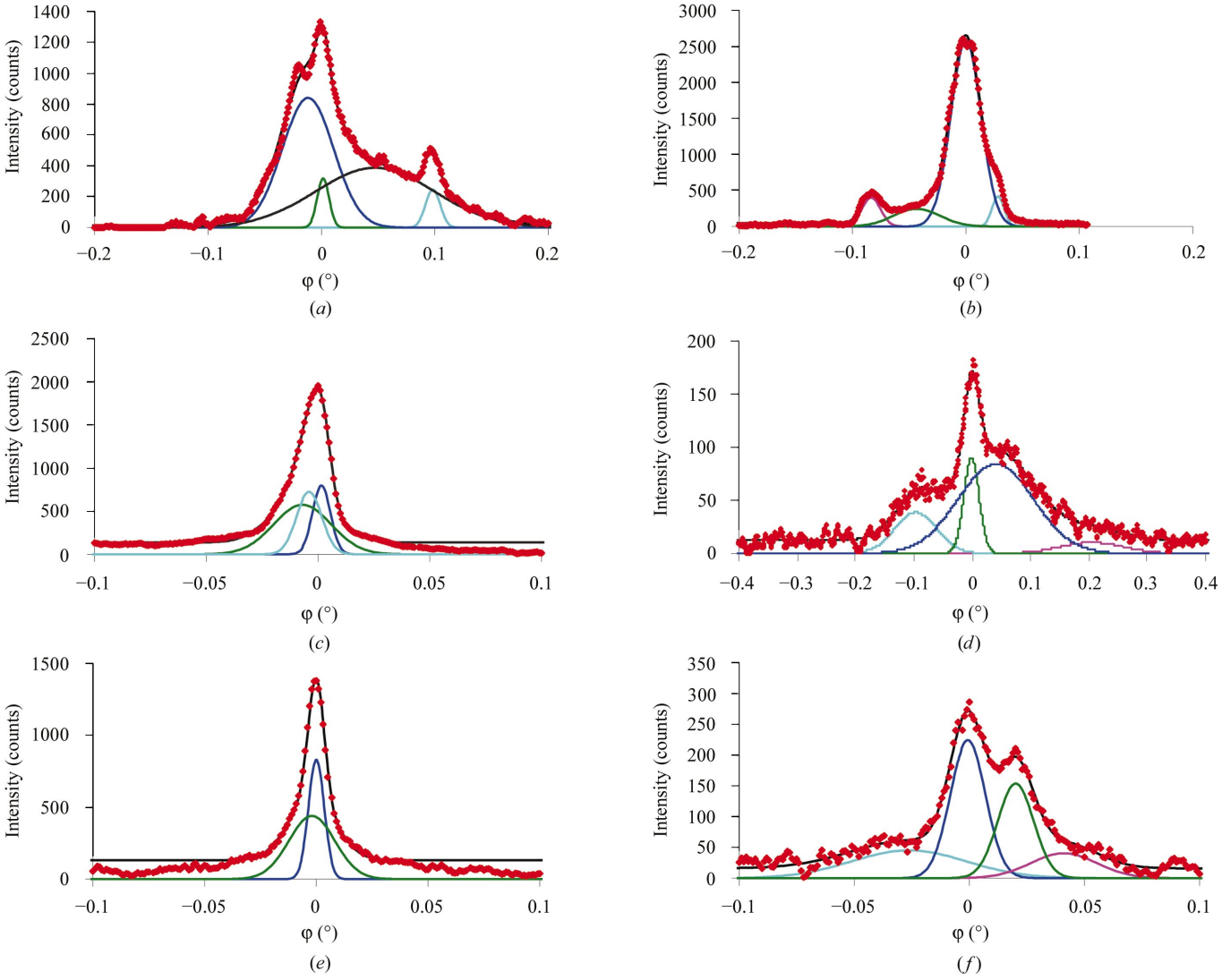

Figure 4
Representative reflection profiles from rt earth crystals. Reflections were selected that had average resolution and average FWHM mosaicity for that crystal (see Table 2). (*a*) earth1 [−2, 4, 9], d = 3.73 Å, φ_R = 0.051°, η = 0.046°; (*b*) earth2 [−5, 22, −3], d = 3.41 Å, φ_R = 0.033°, η = 0.031°; (*c*) earth3 [8, −4, 9], d = 3.54 Å, φ_R = 0.018°, η = 0.016°; (*d*) earth4 [7, −11, −6], d = 4.51 Å, φ_R = 0.073°, η = 0.069°; (*e*) earth5 [−20, 1, 0], d = 3.64 Å, φ_R = 0.012°, η = 0.011°; (*f*) earth6 [14, −1, −3], d = 4.83 Å, φ_R = 0.037°, η = 0.031°.

Table 2
Diffraction and crystal mosaicity statistics for rt insulin crystals.

Crystal	Crystal volume (mm^3)	Avg† d (Å)	Highest resolution reflection measured (Å)	η_{avg} FWHM‡ (°)	η_{avg} FWQM‡ (°)	No. reflections analyzed	Avg. max. peak intensity§ (counts)	Unit-cell volume¶ (nm^3)
Microgravity-grown insulin crystals								
μ*g*1	0.31	2.81	1.63	0.004 (0.001)	0.007 (0.002)	425	8562	201
μ*g*2	0.42	2.77	1.63	0.007 (0.005)	0.009 (0.007)	190	8236	200
μ*g*3	0.25	2.89	1.59	0.006 (0.003)	0.009 (0.005)	118	8404	202
μ*g*4	0.47	2.81	1.54	0.003 (0.001)	0.005 (0.002)	544	15352	199
μ*g*5	2.04	2.87	1.58	0.004 (0.002)	0.007 (0.004)	516	6731	204
μ*g*6	1.25	2.83	1.55	0.003 (0.001)	0.005 (0.002)	483	6961	201
Average				0.005 (0.002)	0.007 (0.002)			201 (2)
Earth-grown insulin crystals								
earth1	0.04	3.89	2.10	0.035 (0.018)	0.076 (0.034)	96	554	198
earth2	0.01	3.51	1.93	0.035 (0.015)	0.058 (0.019)	20	880	201
earth3	0.02	3.48	1.73	0.016 (0.006)	0.029 (0.011)	191	824	205
earth4	0.03	6.67	3.32	0.063 (0.025)	0.118 (0.021)	4	136	207
earth5	0.02	3.70	2.13	0.013 (0.004)	0.024 (0.007)	95	374	200
earth6	0.02	4.96	2.91	0.026 (0.010)	0.048 (0.018)	34	299	197
Average				0.031 (0.018)	0.059 (0.035)			201 (4)

† This average was used for selecting representative reflection profiles in Figs. 3 and 4. ‡ Standard deviations are given in parentheses. § The average peak height for all reflections of the crystal normalized for a 2 s exposure time is reported. For rt earth crystals, normalized reflections with I_{max} >100 counts were analyzed. For rt μ*g* crystals, normalized reflections with I_{max} > 150 counts were analyzed. These filters are more stringent than those previously reported (Borgstahl *et al.*, 2001), but allow the direct comparison of diffraction resolution. ¶ Unit-cell volumes were calculated from dimensions obtained by processing the coarse images with *MOSFLM*.

Table 3
Diffraction and crystal mosaicity statistics for cryo insulin crystals.

Crystal	Crystal volume† (mm^3)	Avg‡ d (Å)	Highest resolution reflection measured (Å)	η_{avg} FWHM‡§ (°)	η_{avg} FWQM§ (°)	No. reflections analyzed	Avg. max. peak intensity¶ (counts)	Unit-cell volume¶ (nm^3)
Microgravity-grown insulin crystals								
cr-μ*g*7		3.76	1.92	0.234 (0.035)	0.468 (0.058)	127	1852	191
cr-μ*g*8		3.01	1.66	0.208 (0.043)	0.317 (0.068)	601	3766	189
cr-μ*g*9		4.70	2.30	0.210 (0.059)	0.326 (0.084)	272	498	189
Average				0.217 (0.012)	0.370 (0.069)			190 (1)
cr-μ*g*6 ††	1.25	4.05	2.09	0.185 (0.051)	0.288 (0.080)	288	854	189
Earth-grown insulin crystals								
cr-earth7		4.11	2.05	0.324 (0.055)	0.514 (0.088)	630	485	194
cr-earth8		4.42	2.17	0.198 (0.055)	0.306 (0.071)	311	518	196
cr-earth9		4.39	2.20	0.215 (0.053)	0.354 (0.066)	116	464	190
Average				0.246 (0.068)	0.391 (0.109)			193 (3)
cr-earth4††	0.03	5.68	2.75	0.166 (0.060)	0.335 (0.108)	64	826	189

† The dimensions of crystals cr-μ*g*7–9 and cr-earth7–9 were not measured. Their sizes were similar to the rt crystals (Table 2). ‡ This average was used for selecting representative reflection profiles in Figs. 5 and 6. § Standard deviations are given in parentheses. ¶ The average maximum peak height for all reflections of the crystal was normalized for a 2 s exposure time. For cryo μ*g* and earth crystals, normalized reflections with I_{max} > 150 counts were analyzed. †† Room-temperature data were collected on μ*g*6 and earth4 crystals prior to cryocooling; therefore, they are not included in the average. The μ*g*6 crystal was composed of two domains (Fig. 3*f*) and the earth4 crystal was composed of four domains (Fig. 4*d*) † Unit-cell volumes were calculated from dimensions obtained by processing the coarse images with *MOSFLM*.

tically significant when tested with a Student's t-test ($t = 0.7022$, two-tailed $P = 0.5212$). Clearly, the gain in crystal quality obtained through μ*g* growth appears to be offset by the effects of cryocooling. One of the cryo μ*g* crystals also diffracted beyond the edge of the detector and the resolution limit for cryo earth crystals ranged from 2.05 to 2.20 Å. This is similar to the trend observed at rt.

Differences in mosaicity between the two samples of cryo crystals are notable when the spread in the data is examined. Individual cryo earth η_{avg} FWHM had a range of 0.126° and extended from 0.198 to 0.324° (Table 3). In comparison, individual cryo μ*g* crystals η_{avg} FWHM had a range of only 0.026°, varying from 0.208 to 0.234°. These data indicate that cryo μ*g* reflections were more internally homogeneous in η than those from the earth crystals.

The average difference between mosaicity measurements of symmetry-related reflections within individual crystals, $\text{Avg}\Delta\eta_{sym}$, also show differences between the cryocooled μ*g* and earth crystals (Table 4). This statistic is used here in a similar fashion as the R value between symmetry-related reflections, R_{sym}, is traditionally used as an indicator of data quality. Absorption and anomalous effects were minimized by using a wavelength of 1 Å. If it is assumed that in the better crystal the symmetry-related reflections should have similar mosaicity, then the $\text{Avg}\Delta\eta_{sym}$ values should be another indicator of diffraction quality. As for R_{sym}, a smaller value of $\text{Avg}\Delta\eta_{sym}$ values would indicate better data. Table 4 summarizes a comparison of the $\text{Avg}\Delta\eta_{sym}$ within individual data sets. Only two 1° swaths of data were collected, so the number of available symmetry-related reflections within a given crystal was limited. The $\text{Avg}\Delta\eta_{sym}$ values are 2.5 times smaller for the cryo μ*g* crystals. In Table 4, a larger spread in the standard deviation of $\Delta\eta_{sym}$ values for the earth data compared with the μ*g* data is also noted. These data support the observation that the cryo μ*g* mosaicity data have better internal agreement than the earth data.

The crystals were oriented randomly during data collection and the same reflections were not measured for each crystal. Therefore, pairs of μ*g* and earth crystals that happened to share a subset of symmetry-related reflections were compared using the $\Delta\eta_{merge}$ statistic (Table 5). This statistic can be likened to the R_{merge} statistic that is calculated to measure isomorphism between a pair of crystals. In Table 5, the average η for a subset of symmetry-related reflections shared by a crystal pair was calculated for each crystal in the pair and then

Table 4
Mosaicity differences between symmetry-related reflections within individual cryo insulin crystals.

Crystal	Avg. η FWHM† (°)	Avg$\Delta\eta_{sym}$†	No. symmetry-related reflections
Microgravity-grown insulin crystals			
cr-μ*g*8	0.202 (0.033)	0.039 (0.019)	17
cr-μ*g*9	0.186 (0.049)	0.048 (0.032)	54
average	0.194	0.044	
cr-μ*g*6	0.179 (0.039)	0.059 (0.043)	16
Earth-grown insulin crystals			
cr-earth7	0.312 (0.068)	0.082 (0.076)	195
cr-earth8	0.231 (0.159)	0.141 (0.158)	86
Average	0.272	0.112	

† Room-temperature data were collected on crystal μ*g*6 prior to cryocooling; therefore, it is not included in the average. For this analysis, the data were not normalized to 2 s exposure time before the filter of 150 counts was applied to I_{max}. Standard deviations are given in parentheses.

Table 5
Mosaicity differences of symmetry-related reflections between microgravity and earth-grown cryo insulin crystals.

Crystal	Avg. η FWHM† (°)	$\Delta\eta_{merge}$‡	No. symmetry-related reflections
cr-μ*g*8	0.202 (0.039)		
		−0.085	230
cr-earth7	0.287 (0.076)		
cr-μ*g*6	0.188 (0.074)		
		−0.071	42
cr-earth8	0.259 (0.121)		
cr-μ*g*9	0.224 (0.066)		
		−0.035	104
cr-earth8	0.259 (0.159)		
cr-μ*g*6	0.154 (0.020)		
		−0.124	18
cr-earth8	0.279 (0.180)		

† Standard deviations are given in parentheses. For this analysis, the data were not normalized to 2 s exposure time before the filter of 150 counts was applied to I_{max}. ‡ $\Delta\eta_{merge}$ = Avg$\Delta\eta_{sym}$ top crystal − Avg$\Delta\eta_{sym}$ bottom crystal. Negative values indicate the bottom crystal had a worse Avg$\Delta\eta_{sym}$ than the top crystal. To identify symmetry-related reflections between data sets, the interprocess communication feature in *BEAM-ish* 2.0 was used (Lovelace & Borgstahl, 2003).

the differences taken to give $\Delta\eta_{merge}$. For each pair of crystals compared, the μ*g* Avg$\Delta\eta_{sym}$ (top crystal) values were subtracted from the earth Avg$\Delta\eta_{sym}$ values (bottom crystal). Therefore, negative values of $\Delta\eta_{merge}$ indicate that the earth crystals had a worse $\Delta\eta_{sym}$ than the μ*g* crystals for this subset of reflections. The $\Delta\eta_{merge}$ values ranged from −0.035 in the best comparison to −0.124 for the worst comparison. From Table 4, the best Avg$\Delta\eta_{sym}$ value was 0.039 for the best cryo μ*g* crystal (cr-μ*g*8). Therefore, the $\Delta\eta_{merge}$ of −0.035 for cr-μ*g*9 and cr-earth8 can be judged as having borderline significance. However, the $\Delta\eta_{merge}$ of −0.124 for cr-μ*g*6 and cr-earth8 is three times higher than Avg$\Delta\eta_{sym}$(cr-μ*g*8) and is a significant difference in the measurement of symmetry-related reflections. This analysis further supports the observation that the μ*g* diffraction data are more internally consistent than the earth data.

3.4. Effect of cryocooling on reflection profiles, domain structure and diffraction resolution

The cryo μ*g* crystals had a similar number of mosaic domains as the rt μ*g* crystals (Figs. 3 and 5). Two cryo μ*g* crystals were described by two Gaussian curves and one cryo μ*g* crystal needed only one curve. As observed for the rt earth crystals (Fig. 4), the cryo earth crystals were composed of 3–4 mosaic domains (Fig. 6). Therefore, cryocooling does not appear to increase the number of mosaic domains (Fig. 2, center arrow).

The trends in the crystal mosaicity and intensity data (Table 3) correlate well with the quality of the observed cryo reflection profiles (Figs. 5 and 6). For example, cr-μ*g*8 had the lowest average η at FWHM and FWQM (Table 3) and the lowest Avg$\Delta\eta_{sym}$ (Table 4). The corresponding reflection profiles for cr-μ*g*8 could be described by a single Gaussian curve (Fig. 5*b*). It is interesting that of all the cryo crystals, cr-μ*g*8 also diffracted to the highest resolution and had the highest average maximum peak intensity (Table 3). Part of the gain in maximum peak height is a consequence of the crystal size, but in Fig. 5(*b*) it can be seen that the reflections from this crystal also had an improved signal-to-noise ratio and could be described by a single Gaussian. Unfortunately, the effects of crystal size and mosaicity on maximum peak height cannot be separated, as the crystal volume illuminated by the X-ray beam for each swath of fine φ-sliced data for the cryo crystals is not known precisely. For most crystals, the X-ray beam was smaller than the crystal and this reduced the effect of crystal volume differences on peak height. The final conclusion from the profiles (Figs. 5 and 6) is that it is possible to cryocool nearly perfect crystals and retain a single resolvable mosaic domain. When a single domain is retained after cryocooling, the signal-to-noise ratio of the data is improved by increasing the peak height of the reflections, making the weaker and higher resolution data easier to measure. A bonus effect is obtained if the single-domain structure is retained in a large crystal, as in the μ*g* case.

3.5. An individual case study

An additional experiment was performed using one earth and one μ*g* crystal. For each crystal, rt and cryo fine φ-sliced data were collected sequentially (Table 1). For the cryo data collection the crystals were carefully removed from the capillary by manipulating the mother-liquor plugs at either side of the crystal. The crystals were then treated as described in §2.2. The earth and μ*g* data show similar trends (earth4 and μ*g*6, Table 2; cr-earth4 and cr-μ*g*6, Table 3). The earth4 crystal was composed of at least four mosaic domains (Fig. 4*d*), had the highest rt η FWHM measured at 0.063° and its η was increased threefold by cryocooling (Table 3). The μ*g*6 crystal was described by two domains (Fig. 3*f*) and its rt η at FWHM of 0.003° was raised 62-fold to 0.185° by cryocooling (Table 3). These data confirm the trends noted above by studying average values from different crystal samples. Crystal μ*g*6 had significantly more measurable reflections than earth4, so it was analyzed in detail. From these data, the effects of cryocooling

on domain broadening and separation can be seen and resolved by curve fitting (Figs. 1*b* and 1*c*).

The mosaic domain structure of μ*g*6 was analyzed in terms of mosaic domain theory (illustrated in Fig. 2). The effects of cryocooling on mosaic domain width and separation were extracted by fitting all the reflection profiles with Gaussian curves (examples are available as supplementary material[1]), deconvolution of the data (Table 6) and detailed study of three-dimensional reflection topographs (Fig. 7). At rt, the average η values of each domain were 0.003 and 0.001°, with a separation of 0.003° (Table 6). Upon cryocooling, the average η of each domain increased to 0.228–0.293 and 0.110–0.145°, respectively. The angular separation of these domains also increased to 0.101–0.132°. Therefore, the increase in mosaicity caused by cryocooling is caused by both an increase in the mosaicity of individual mosaic domains and by an increase in the angular separation in φ of the mosaic domains (Fig. 2, right). An increase in the number of mosaic domains was not observed (Fig. 2, center arrow).

X-ray topography is an imaging technique that is essentially the visualization of the components of the crystal that contribute to the reflection at one point in the reflection profile. It has been used to study how irregularities in the lattice cause locally changing diffracted intensities (contrast) within individual reflections (Boggon *et al.*, 2000). Fine-grained nuclear emulsions or X-ray film are usually used. In

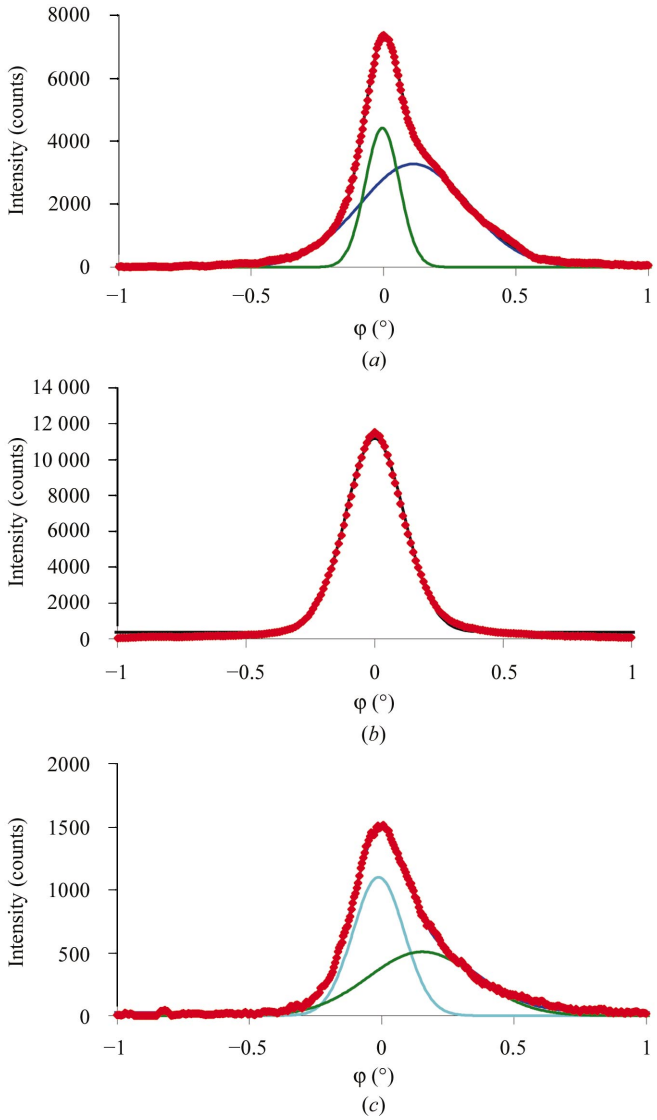

Figure 5
Representative reflection profiles from cryo μ*g* crystals. Reflections were selected that had average resolution and average FWHM mosaicity for that crystal (see Table 3). (*a*) cr-μ*g*7 [−16, 19, 4], d = 3.63 Å, φ_R = 0.243°, η = 0.237°; (*b*) cr-μ*g*8 [16, 4, −6], d = 3.15 Å, φ_R = 0.262°, η = 0.174°; (*c*) cr-μ*g*9 [3, −15, −3], d = 4.66 Å, φ_R = 0.291°, η = 0.249°.

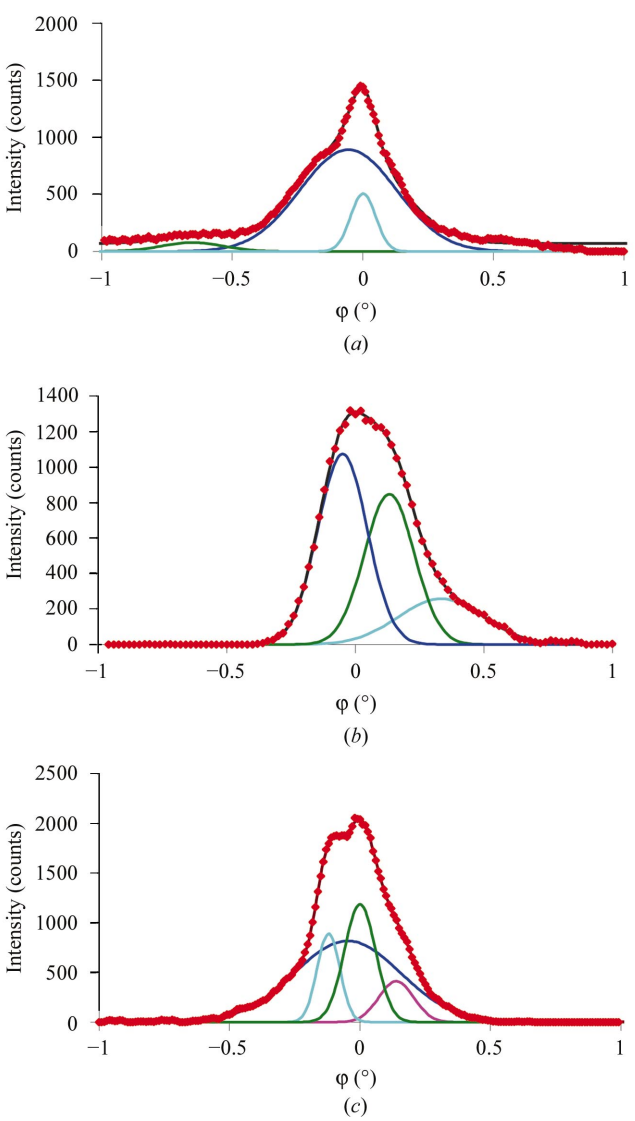

Figure 6
Representative reflection profiles from cryo earth crystals. Reflections were selected that had average resolution and average FWHM mosaicity for that crystal (see Table 3). (*a*) cr-earth7 [−4, −5, 7], d = 4.30 Å, φ_R = 0.320°, η = 0.305°; (*b*) cr-earth8 [3, −5, −7], d = 4.53 Å, φ_R = 0.196°, η = 0.195°; (*c*) cr-earth9 [10, −12, −5], d = 4.49 Å, φ_R = 0.318°, η = 0.298°.

Table 6
Analysis of mosaic domain structure in μg6 crystal.

Owing to the potential for error in curve fitting from extreme reflection broadening by the Lorentz effect, data from the horizontal sectors of the detector were not used. The crystal was larger than the beam; therefore, the two orthogonal swaths of data were kept on separate lines as they may be from different regions of the crystal. The crystal orientation at each temperature was random and a different group of reflections was collected at each temperature. For cryocooled data, Gaussian 1 curves (*e.g.* see figure in supplementary material, green curve) were in general shorter and below the total FWHM of the complete reflection profile.

	Avg. η (std)	Gaussian 1, avg. η (std)	Gaussian 2, avg. η (std)	Separation, avg. $\varphi1 - \varphi2$ (std)
Room temperature				
163 reflections	0.003 (0.001)	0.003 (0.002)	0.001 (0.001)	0.003 (0.002)
153 reflections	0.002 (0.001)	0.003 (0.002)	0.001 (0.001)	0.003 (0.002)
Cryocooled				
173 reflections	0.195 (0.036)	0.228 (0.072)	0.110 (0.051)	0.101 (0.087)
35 reflections	0.223 (0.048)	0.293 (0.073)	0.145 (0.058)	0.132 (0.126)

Table 7
Significant steric conflicts between the rt structure of the first four residues of monomer B2 with the cryo crystal lattice.

The coordinates for symmetry-related molecules of 4ins and 1mso, respectively, were generated with *PDBSET* from the *CCP*4 software suite (Collaborative Computational Project, Number 4, 1994) and then the distances between the room-temperature N-terminal four-residue peptide and the cryo hexamer-forming interface were observed with the tools available in *XtalView* (McRee, 1992). Only contacts deviating by more than 0.1 Å from the ideal van der Waals distance are listed. A dash indicates that no significant steric conflicts were noted for that residue.

Rt residues	Rt atom	Cryo lattice residue	Cryo lattice atom	Distance (Å)	Ideal VDW distance (Å)	Deviation from ideal (Å)	Equivalent distances to cryo lattice for B.1 (Å)
Phe1B.2	—	—	—	—	—	—	
Val2B.2	$C^{\gamma2}$	CysB19.1	O	2.77	3.22	0.45	3.86
Val2B.2	$C^{\gamma2}$	CysB19.1	C	2.83	3.40	0.57	3.93
Val2B.2	$C^{\gamma2}$	GlyB20.1	N	2.76	3.25	0.49	4.03
Val2B.2	$C^{\gamma2}$	GlyB20.1	C^{α}	2.61	3.40	0.79	4.00
Asn3B.2	—	—	—	—	—	—	
Gln4B.2	—	—	—	—	—	—	

this case, the pixel size of the Quantum-4 CCD detector was too large to study the reflections in detail, but the fine slicing provided excellent resolution normal to the detector face. Three-dimensional topographs were reconstructed in order to observe the gross effect of cryocooling and annealing on μg6 reflections (Fig. 7). The cryo topographs are dramatically elongated (Fig. 7*b*, center) when compared with the spherical rt topographs (Fig. 7*a*, center). When transformed into reciprocal (*hkl*) space, the rt reflection is very narrow (Fig. 7*a*, right) and the cryo reflection is broad (Fig. 7*b*, right). This analysis shows how the observed increases in crystal mosaicity caused by cryocooling are propagated into *hkl* space.

3.6. Effect on insulin structure

To understand the short-range changes in protein structure resulting from cryocooling, the 1.5 Å resolution rhombohedral rt porcine insulin structure (PDB code 4ins) was compared with the 1.0 Å cryo rhombohedral human insulin structure (PDB code 1mso). High-resolution structures at rt and cryo in the rhombohedral space group and from the same species were not available for comparison. Porcine insulin differs from human insulin only at residue 30 in the B chain, which is Ala for porcine and Thr for human. This difference does not appear to affect the large structural changes at the N-terminus (Smith *et al.*, 2003). The rt unit-cell dimensions were $a = b = 82.5$, $c = 34.0$ Å, with a unit-cell volume of 200.4 nm^3. The cryo unit-cell dimensions shrank to $a = b = 81.29$, $c = 33.71$ Å, with a unit-cell volume of 192.9 nm^3. Therefore, cryocooling caused the volume of the unit cell to decrease by 7.5 nm^3 or 3.9% (Smith *et al.*, 2003).

One insulin molecule is composed of an A chain of 21 amino acids and a B chain of 30 amino acids. For the *R*3 crystals, the asymmetric unit of the crystal is composed of an insulin dimer $(AB)_2$ (Fig. 8*a*). The standard insulin nomenclature will be used here, where monomers in the first AB dimer in the asymmetric unit are referred to by a decimal .1 (*e.g.* GlyA1.1 or PheB1.1) and the monomers in the second AB dimer are referred to by .2 (*e.g.* GlyA1.2 or PheB1.2). The unit cell contains three $(AB)_2$ dimers aggregated to form a hexamer around two Zn ions (Baker *et al.*, 1988).

The structural changes caused by cryocooling are summarized in a table in the supplementary material. In general, the overall structural effects of cryocooling are similar to those seen in other protein crystals (Juers & Matthews, 2001). A negative fractional change in the radius of gyration with cooling (ΔR_g) and an increase in the number of intramolecular contacts indicate that the insulin molecule has contracted. Cryoinduced shrinkage of the unit cell caused a 17% increase in the number of intermolecular crystal contacts. The B30Ala→Thr substitution and differences in modeled dual conformers probably accounts for some of the cryo-induced increase, but not all.

Cryocooling and its associated unit-cell shrinkage appears to have had large structural consequences. Smith and co-workers observed differences at the N-terminus of the B chain of monomer 2 and this change is re-examined here (Fig. 8) (Smith *et al.*, 2003). In this analysis, there was no need to superimpose the structures since the cryo and rt structures are in essentially the same orientation and only significantly differ at the N-terminus of subunit B.2 (see Fig. 8*a*). The first four residues of the cryo B.2 monomer have moved (C^{α} displacements of 8.4, 5.8, 1.8 and 1.9 Å for residues PheB1.2, ValB2.2, AsnB3.2 and Gln4.2, respectively). For the rt structure, the side chains of PheB1.2 and ValB2.2 are nestled into a hydrophobic pocket that is partially composed of residues from symmetry-related molecules across the hexamer-forming interface but are not completely buried (Fig. 8*b*) (see also Fig. 4 in Smith *et al.*, 2003). For the cryo structure, PheB1.2 and ValB2.2 are out of the hydrophobic pocket and in a more hydrophilic environment that is also near symmetry-related molecules of the crystal lattice. The van der Waals contacts between the rt structure of residues B1.2–B4.2 with the cryo crystal contacts were examined (Fig. 8*c*) and contacts that are

significantly too short are listed in Table 7. There are several significant steric conflicts between the rt side chain of ValB2.2 and the main chain of CysB19.1 and GlyB20.1 across the cryo crystal lattice (Table 7). A similar examination of monomer B.1 did not reveal any bad contacts between the rt structure and the cryo crystal contacts (Table 7, right column). Therefore, the sharp bend at AsnB3.2 and large displacements of PheB1.2 and ValB2.2 probably arise from a steric problem at ValB2.2 caused by cryo-induced shrinkage of the unit cell. This steric conflict-associated movement is reminiscent of the ligand-induced steric conflict between ValFG5 and the heme in the T→R quaternary structure change of hemoglobin (Perutz, 1989). Coordinates for insulin at rt but in the presence of cryoprotectant are not available, so the unlikely possibility that the cryoprotectant has induced these movements cannot be ruled out.

The N-terminus of monomer B.2 is more disordered in the cryo structure. In fact, no density was present for the ring of PheB1.2 and it was not refined (Smith *et al.*, 2003). Disorder can be both spatial and temporal and the refined structure represents an average of the contents of all the unit cells. The temporal component of disorder is minimized by

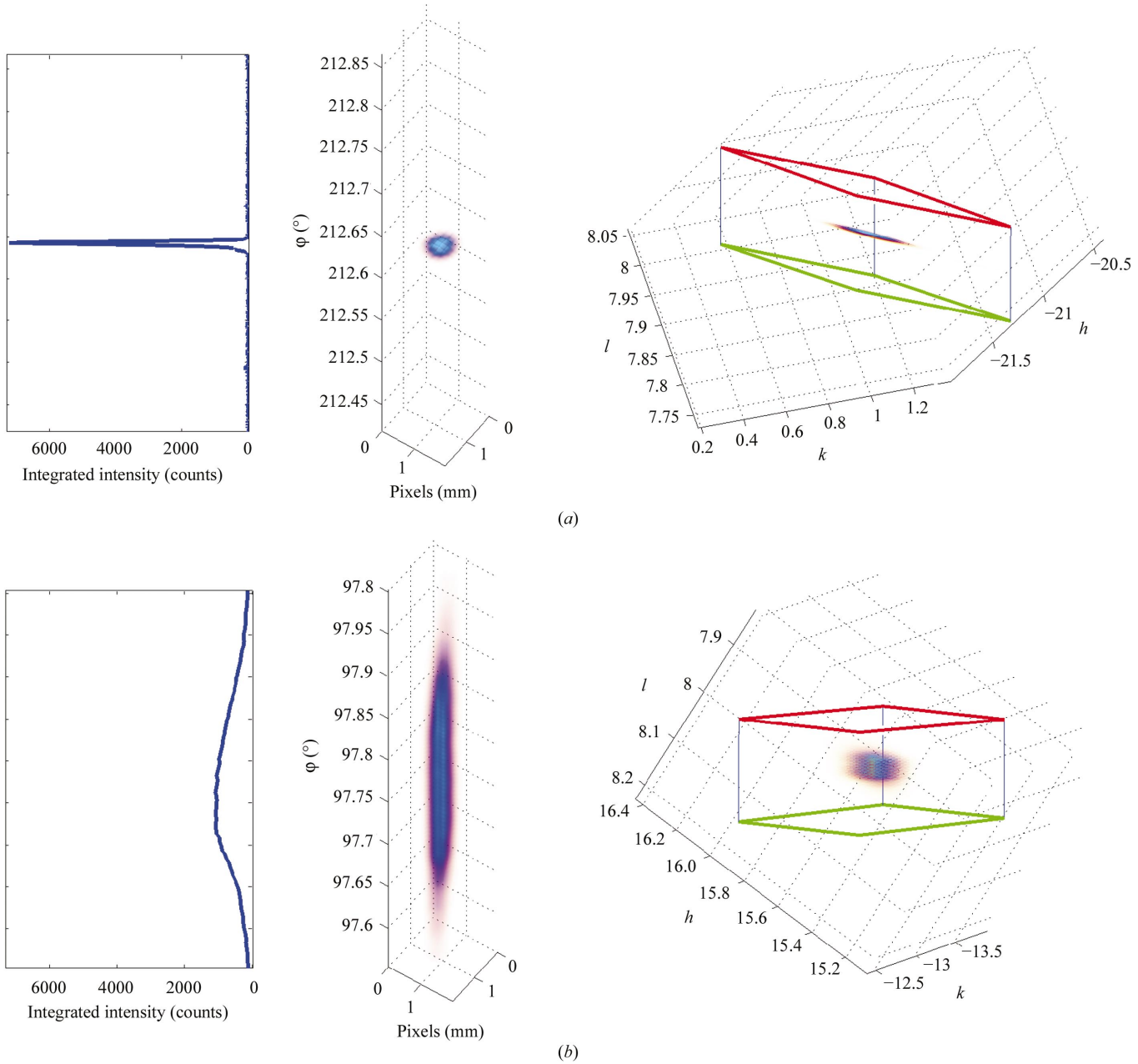

Figure 7
Three-dimensional reflection topographs for (*a*) rt and (*b*) cryo reflections. Reflection profiles (left), reconstructed three-dimensional topographs (middle) and reflection in reciprocal (*hkl*) space (right) are shown. The green lines give the location of the φ_{start} and the red lines the φ_{end} image. The rt reflection in (*a*) looks like a pancake in *hkl* space. This is because no correction was applied for the broadening of the reflection topographs by the point-spread function and pixel size of the CCD detector.

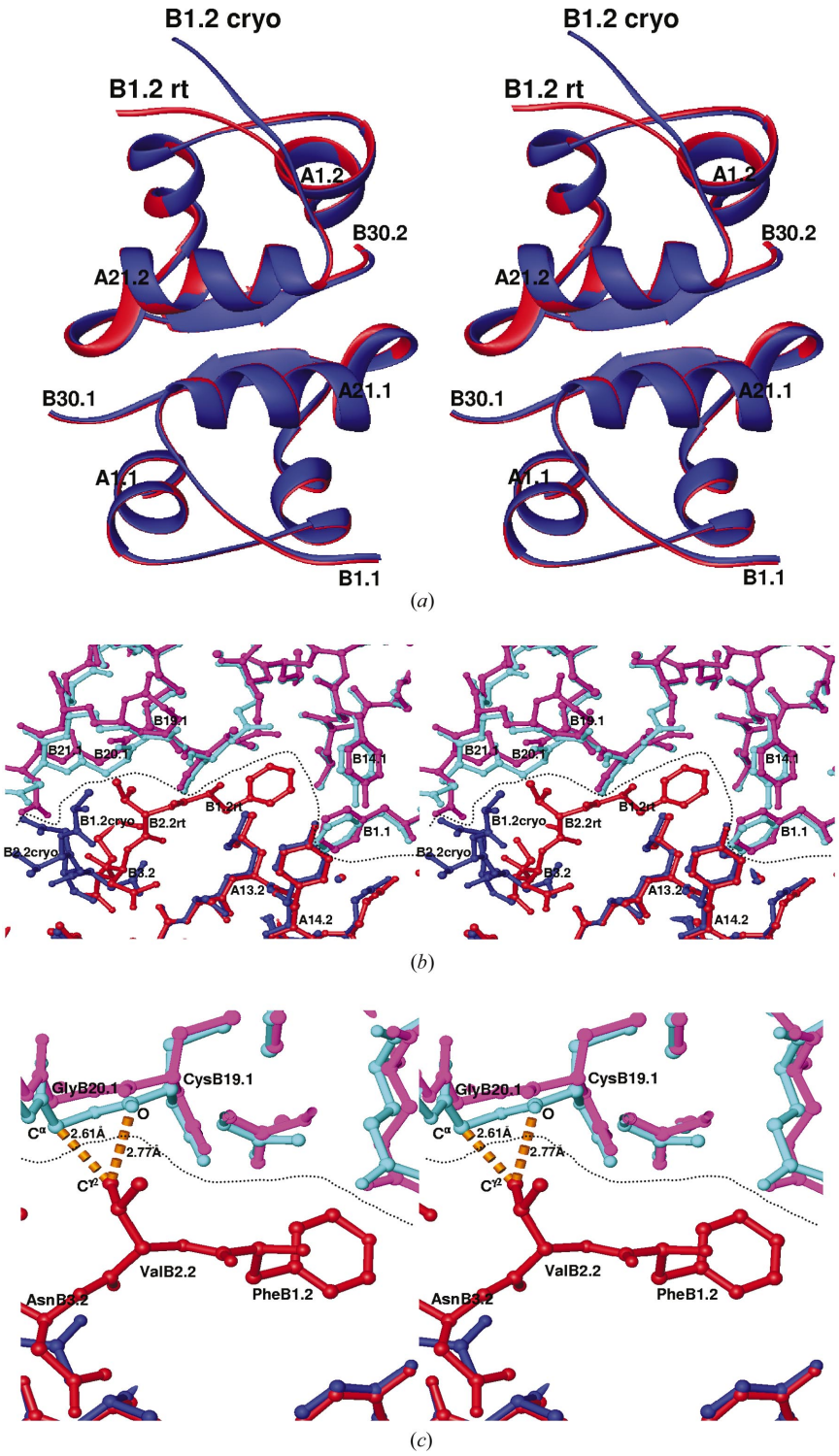

Figure 8
Structural comparison between rt and cryo insulin structures. (*a*) Stereo ribbon drawing of cryo (blue, 1mso) and rt (red, 4ins) insulin asymmetric unit. No superposition was performed. The largest structural differences include four residues at the N-terminus of the B.2 chain, breaking the non-crystallographic symmetry of the dimer of dimers. (*b*) Stereopair of some of the lattice contacts near PheB1.2 and ValB2.2 (blue, cryo; red, rt). A 9 Å slab of the structures is shown. All solvent has been omitted for clarity. A dotted line indicates the border between the asymmetric unit and the symmetry-related molecules (cyan, cry; magenta, rt) that comprise the crystal lattice. (*c*) Magnified view of steric conflicts between rt ValB2.2 structure (red) and the cryo crystal lattice (cyan). Some of the violated van der Waals distances (Table 7) are indicated with orange dashed cylinders. Figures were produced with *RIBBONS* 3.18 (Carson, 1997)

cryocooling; therefore, the N-terminus of monomer B.2 probably has slightly different structures in each unit cell of the crystal.

4. Conclusions

A number of studies have shown that protein crystal growth under μ*g* conditions results in dramatic improvement of the overall crystal quality (Boggon *et al.*, 2000; Kundrot *et al.*, 2001; Ng *et al.*, 1997, 2002; Snell *et al.*, 1995). However, the gain in crystal perfection may be offset by the effects of flash-cooling on the crystal lattice. In the case of the *R*3 insulin crystals studied here, cryocooling largely obliterates the improved long-range order seen in the rt μ*g* crystals and results in a mosaicity similar to the cryocooled ground-grown crystals. It appears that mosaic domains of the μ*g* crystals are preserved, resulting in clearly improved profile shapes compared with the ground crystals. The μ*g* crystals had large volumes, with linear dimensions ranging from 0.4 to 1.8 mm (see Table 1 in Borgstahl *et al.*, 2001) and it is surprising that they cryocooled as well as they did. Here, in both ground and μ*g* crystals, cryocooling increases the mosaicity by increasing the domain misalignment and also by broadening the contribution from each individual domain. However, it seems that stress from the cooling or the cryoprotection protocol does not break up existing domains. The number of domains remains constant.

In terms of short-range order, from analysis of published high-resolution insulin structures the unit cell is found to shrink and the number of intramolecular contacts increases. The N-terminus of one insulin molecule becomes disordered upon cryocooling. This disorder may be a cause of the possible unit-cell variation thought to contribute to the broadened reflections from each domain. This is hard to prove without further experimentation. Contraction of the unit cell may well be the underlying reason for the increase in domain misalignment, as it will leave a boundary region between each domain where differential contraction or expansion could be the cause of the increase in domain misalignment seen in the results.

Finally, it was possible to cryocool a single-domain crystal and retain single but broadened reflection profiles. Such reflections had improved signal-to-noise ratios compared with the reflections from multi-

domain crystals and these superior reflection profiles contributed significantly to the detection and measurement of high-resolution diffraction data.

The overall effect of cryocooling on crystal quality seen here is the broadening of the individual mosaic domains and increased domain misalignment. No increase in the number of domains was observed. Domain broadening probably arises from structural changes which result in unit-cell changes and the increase in domain misalignment may be a secondary effect of unit-cell variations in the individual domains. Whether or not structural changes are induced by cryocooling could therefore be a factor in determining which crystals cryocool without significantly increasing mosaicity.

This work was supported by NASA grants NAG8-1580, NAG8-1380 and NAG8-1836. EHS is a contractor to NASA through BAE Systems Analytical Solutions. We are grateful to M. Pokross for technical assistance during data collection, Eli Lilly for providing the recombinant insulin, Drs W. Pangborn and B. Blessing at the Hauptmann–Woodward Medical Institute (Buffalo, NY) for their advice, help, provision of insulin crystals and the cryocooling protocol, Dr G. D. Smith for providing the cryocooled microgravity T_6 insulin coordinates (1mso) before publication and for critically reading drafts of this manuscript, Dr J. Glenn for activating the crystallization experiment in orbit and Drs M. Long, V. King and L. DeLucas at the University of Alabama in Birmingham for optimizing crystal growth and for pictures of the crystal samples. This work is based upon research conducted at the Stanford Synchrotron Radiation Laboratory, which is funded by the Department of Energy, Office of Basic Energy Sciences. The Biotechnology Program is supported by the National Institutes of Health, National Center for Research Resources, Biomedical Technology Program and the Department of Energy, Office of Biological and Environmental Research.

References

Baker, E. N., Blundell, T. L., Cutfield, J. F., Cutfield, S. M., Dodson, E. J., Dodson, G. G., Hodgkin, D. M. C., Hubbard, R. E., Isaacs, N. W., Reynolds, C. D., Sakabe, K., Sakabe, N. & Vijayan, N. M. (1988). *Philos. Trans. R. Soc. London Ser. B*, **319**, 369–456.

Bellamy, H., Phizackerley, R. P., Soltis, S. M. & Hope, H. (1994). *J. Appl. Cryst.* **27**, 967–970.

Bellamy, H. D., Snell, E. H., Lovelace, J., Pokross, M. & Borgstahl, G. E. O. (2000). *Acta Cryst.* D**56**, 986–995.

Boggon, T. J., Helliwell, J. R., Judge, R. A., Olczak, A., Siddons, D. P., Snell, E. H. & Stojanoff, V. (2000). *Acta Cryst.* D**56**, 868–880.

Borgstahl, G. E. O., Vahedi-Faridi, A., Lovelace, J., Bellamy, H. D. & Snell, E. H. (2001). *Acta Cryst.* D**57**, 1204–1207.

Carson, M. (1997). *Methods Enzymol.* **277**, 493–505.

Chayen, N. E., Snell, E. H., Helliwell, J. R. & Zagalsky, P. F. (1997). *J. Cryst. Growth*, **171**, 219–225.

Colapietro, M., Cappuccio, G., Marciante, C., Pifferi, A., Spagna, R. & Helliwell, J. R. (1992). *J. Appl. Cryst.* **25**, 192–194.

Collaborative Computational Project, Number 4 (1994). *Acta Cryst.* D**50**, 760–763.

Darwin, C. G. (1922). *Philos. Mag.* **43**, 800–829.

Deacon, A., Gleichmann, T., Kalb (Gilboa), A. J., Price, H., Raftery, J., Bradbrook, G., Yariv, J. & Helliwell, J. R. (1997). *J. Chem. Soc. Faraday Trans.* **93**, 4305–4312.

Garman, E. F. & Schneider, T. R. (1997). *J. Appl. Cryst.* **30**, 211–237.

Greenhough, T. J. & Helliwell, J. R. (1982). *J. Appl. Cryst.* **15**, 338–351.

Helliwell, J. R. (1988). *J. Cryst. Growth*, **90**, 259–272.

Helliwell, J. R. (1992). *Macromolecular Crystallography with Synchrotron Radiation*. Cambridge University Press.

Juers, D. H. & Matthews, B. W. (2001). *J. Mol. Biol.* **311**, 851–862.

Kriminski, S., Caylor, C. L., Nonato, M. C., Finkelstein, K. D. & Thorne, R. E. (2002). *Acta Cryst.* D**58**, 459–471.

Kundrot, C. E., Judge, R. A., Pusey, M. L. & Snell, E. H. (2001). *Cryst. Growth Des.* **1**, 87–99.

Leslie, A. G. W. (1999). *Acta Cryst.* D**55**, 1696–1702.

Long, M. M., Bishop, J. B., Nagabhushan, T. L., Reichert, P., Smith, G. D. & DeLucas, L. J. (1996). *J. Cryst. Growth*, **168**, 233–243.

Lovelace, J. & Borgstahl, G. E. O. (2003). *J. Appl. Cryst.* **36**, 1101–1102.

Lovelace, J., Snell, E. H., Pokross, M., Arvai, A. S., Nielsen, C., Xuong, N., Bellamy, H. D. & Borgstahl, G. E. O. (2000). *J. Appl. Cryst.* **33**, 1187–1188.

McRee, D. E. (1992). *J. Mol. Graph.* **10**, 44–46.

Mitchell, E. P. & Garman, E. F. (1994). *J. Appl. Cryst.* **27**, 1070–1074.

Nave, C. (1998). *Acta Cryst.* D**54**, 848–843.

Ng, J. D., Lorber, B., Giegé, R., Koszelak, S., Day, J., Greenwood, A. & McPherson, A. (1997). *Acta Cryst.* D**53**, 724–733.

Ng, J. D., Sauter, C., Lorber, B., Kirkland, N., Arnez, J. & Giegé, R. (2002). *Acta Cryst.* D**58**, 645–652.

Otálora, F., Capelle, B., Ducruix, A. & García-Ruiz, J. M. (1999). *Acta Cryst.* D**55**, 644–649.

Otwinowski, Z. & Minor, W. (2001). *International Tables for Crystallography*, Vol. *F*, edited by M. G. Rossmann & E. Arnold, pp. 226–235. Dordrecht: Kluwer Academic Publishers.

Perutz, M. F. (1989). *Q. Rev. Biophys.* **2**, 139–236.

Powell, H. R. (1999). *Acta Cryst.* D**55**, 1690–1695.

Rodgers, D. W. (1994). *Structure*, **2**, 1135–1140.

Rodgers, D. W. (1997). *Methods Enzymol.* **276**, 183–202.

Smith, G. D., Pangborn, W. A. & Blessing, R. H. (2003). *Acta Cryst.* D**59**, 474–482.

Snell, E. H., Judge, R. A., Crawford, L., Forsythe, E. L., Pusey, M. L., Sportiello, M., Todd, P., Bellamy, H., Lovelace, J., Cassanto, J. M. & Borgstahl, G. E. O. (2001). *Cryst. Growth Des.* **1**, 151–158.

Snell, E. H., Judge, R. A., Larson, M. & van der Woerd, M. J. (2002). *J. Synchrotron Rad.* **9**, 361–367.

Snell, E. H., Weisgerber, S., Helliwell, J. R., Weckert, E., Holzer, K. & Schroer, K. (1995). *Acta Cryst.* D**51**, 1099–1102.

Teng, T.-Y. (1998). *J. Appl. Cryst.* **31**, 252–257.

Wormington, M., Panaccione, C., Matney, K. M. & Bowen, D. K. (1999). *Philos. Trans. R. Soc. London Ser. A*, **357**, 2827–2848.